第 43 卷 第 21 期/2023 年 11 月/光学学报 研究论文

光学学报

基于测量不确定度的视觉惯性自适应融合算法

黄新欣，任永杰*，马可瑶，牛志远

天津大学精密测试技术及仪器国家重点实验室，天津 300072

摘要 针对环境复杂的工业现场定位精度低、适应性差、鲁棒性低等问题，提出一种基于测量不确定度的视觉惯性自适应融合算法，分析基于隐函数模型的视觉定位测量不确定度，并依据视觉定位测量不确定度自适应调整卡尔曼滤波模型中的参数，校正视觉观测偏差，增强视觉惯性融合定位算法在不同观测条件下的鲁棒性。利用精密三轴转台及激光跟踪仪 T-mac 位姿测量系统对所提融合定位算法的定位精度进行实验验证。实验结果表明，相比传统扩展卡尔曼滤波方法，所提方法能满足视觉观测较差条件下的准确定位需求。

关键词 测量；卡尔曼滤波；不确定度分析；视觉惯性融合；位姿测量

中图分类号 TP23 **文献标志码** A **DOI**：10.3788/AOS230851

1 引 言

近年来，随着计算机视觉、图像处理、数据融合等技术的发展，视觉测量广泛应用于现代工业各领域[1]，其中在多种传感器融合的位姿视觉测量中，视觉惯性技术使用频率最高，发展最快[2]，广泛应用在同时定位与地图构建[3]、空间位姿测量[4]等领域。惯性测量单元（IMU）以较高的频率测量自身运动的加速度和角速度，通过连续时间积分得到载体位姿，其响应速度快、动态性能好、短时精度高。在复杂的工业测量环境中，IMU 能很好地提升视觉定位的鲁棒性[5]。智能制造概念[6]的提出，使得融入式测量逐渐成为制造领域的发展趋势。融入式测量技术指人机共融的测量方式[7]，在保证测量精度的前提下，充分利用人对复杂环境的信息综合处理能力和机器的精确信息感知、高速解算能力，改进在复杂测量场景中测量人员和测量设备的交互方式，大大提升装备制造和测量的效率[8]。

视觉惯性融合算法分为基于滤波的方法和基于优化的方法[9]。这两种方法按照是否把图像特征信息加入状态向量可进一步分为紧耦合方法和松耦合方法。基于优化的方法通常使用紧耦合，根据视觉观测残差和 IMU 测量残差列出代价函数，构建非线性最小二乘问题。VINS-Mono[10]、ORB-SLAM[11]和 OKVIS[12]是典型的优化算法。紧耦合滤波将图像特征添加到状态向量中，典型算法有 MSCKF[13]和 ROVIO[14]等。松耦合滤波的视觉传感器和惯性传感器分别独立测量，基于卡尔曼滤波框架融合数据，典型的算法有 SSF[15]、MSF[16]等。由于 IMU 的高测量频率，基于优化的方法和紧耦合滤波需要大量计算。松耦合滤波由于线性近似误差存在，精度较低，但其计算快、效率高、易扩展，具有重要的应用价值，尤其在实时性要求高的应用场景中。目前，视觉惯性定位仍处于滤波和优化并存的阶段[17]。实现高精度的视觉惯性融合需要获取准确的多相机内外参及多相机和 IMU 外参，各传感器的标定结果会直接影响视觉惯性融合定位结果。对于多传感器内参标定，Wang 等[18]利用单个圆柱体目标同时校准相机和线结构光传感器内参，Zhu 等[19-20]提出了一种基于消失点几何约束的最小拟合误差的变焦透镜校正方法和一种基于最优偏振信息的相机标定方法；对于多传感器外参标定，Eckenhoff 等[21]利用 MSCKF 算法对多相机和 IMU 的外参进行了在线估计，Furgale 等[22]开发了传感器标定工具 Kalibr，基于连续时间批量估计和最大似然理论，估计多传感器之间的位姿。

为了完成航天器、船体等大型结构复杂装备的实时装配定位任务，本文以可穿戴头盔为载体，结合融入式测量技术，通过三轴精密转台标定视觉惯性系统[23]，采用松耦合滤波融合视觉和惯性信息，实时得到测量人员的全局位姿估计，进而配合手持式测靶实现对目标物体的测量。全局位姿精度对目标物体测量精度有直接影响，传统基于滤波的方法实现高精度定位依赖良好的视觉观测条件，但在复杂的工业场景下难以保证。为解决复杂工业环境中视觉观测条件差带来的精度低、适应性差、鲁棒性低等问题，本文提出了一种基于测量不确定度的视觉惯性自适应融合算法。针对视

收稿日期：2023-04-20；**修回日期**：2023-05-25；**录用日期**：2023-06-08；**网络首发日期**：2023-06-28

基金项目：国家自然科学基金（52127810，51721003）、天津市自然科学基金（21JCZDJC00470）

通信作者：*yongjieren@tju.edu.cn

觉观测条件差的情况，通过求解视觉定位测量不确定度，动态调整视觉传感器和惯性传感器数据融合的权值，解算最终位姿，并搭建了实验平台对定位算法的可行性和精度进行了验证。

2 融入式测量定位系统及算法

2.1 融入式测量定位系统结构设计

所述融入式测量定位系统如图 1 所示，以可穿戴头盔为载体，集成同步触发模块、投影显示模块、局部测量模块和全局定位模块。局部测量模块中利用前端测量相机拍摄手持式测靶测量目标物体，再根据全局定位模块提供的全局位姿，解算目标物体的全局参数，经投影显示模块将测得信息投影到目标位置，为现场安装及测量提供帮助。

头盔后端安装 3 台无公共视场的全局定位相机，相机拍摄全局控制场中已知坐标的全局控制板，基于点特征构建 Perspective-n-Point(PnP)问题，实现位姿视觉测量。同时，头盔上方固定 IMU，用于测量运动过程中的三轴加速度和三轴角速度。自适应融合定位

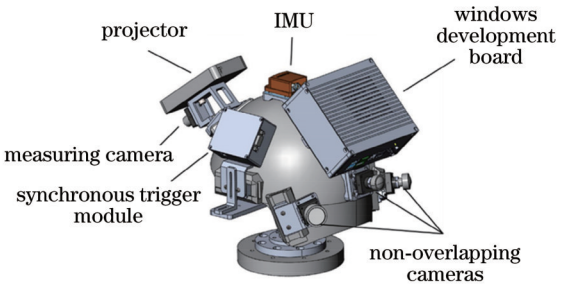

图 1 融入式测量定位头盔

Fig. 1 Immersive positioning and measuring helmet

算法流程如图 2 所示，分两个线程进行。多相机和 IMU 通过同步触发模块输出特定频率的方波实现同步外触发，相机位姿初始化后给 IMU 提供初始位姿，然后利用 IMU 预测的位姿进行特征点匹配并优化求解。对于每一时刻的相机位姿，求解其视觉定位测量不确定度，根据视觉定位测量不确定度动态调节卡尔曼滤波状态更新的权值，实现不同测量环境下的视觉惯性自适应融合定位。

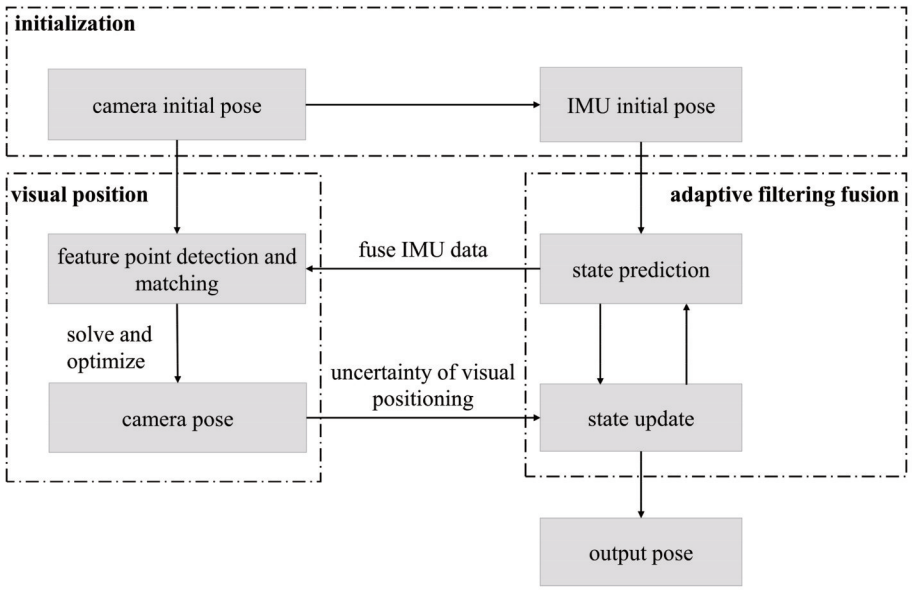

图 2 自适应滤波融合定位算法的流程

Fig. 2 Flow chart of the adaptive filtering fusion positioning algorithm

2.2 视觉定位测量不确定度模型

相机六自由度(6DOF)位姿测量误差包括相机内外参数标定误差、全局控制点位置误差及像点提取误差等。其中，多相机内外参数通过精密三轴转台得到精确标定。基于空间后方交会原理解算相机的 6DOF 位姿，由共线方程可知，全局控制点位置误差和像点提取误差直接影响求解结果。本文采用参数协方差表征被测量不准确程度，将全局控制点位置误差和像点提取误差作为不确定度传播模型的输入量，可得到输出量，即相机 6DOF 位姿测量不确定度[24]，即视觉定位测量不确定度。根据小孔成像模型，相机拍摄全局控制点的重投影误差(e_{xi}, e_{yi})表示为

$$\begin{cases} e_{xi} = u_i - u_0 - \dfrac{f}{d_x}\dfrac{r_1 X_{Wi} + r_2 Y_{Wi} + r_3 Z_{Wi} + t_1}{r_7 X_{Wi} + r_8 Y_{Wi} + r_9 Z_{Wi} + t_3} \\ e_{yi} = v_i - v_0 - \dfrac{f}{d_y}\dfrac{r_4 X_{Wi} + r_5 Y_{Wi} + r_6 Z_{Wi} + t_2}{r_7 X_{Wi} + r_8 Y_{Wi} + r_9 Z_{Wi} + t_3} \end{cases}, \quad (1)$$

式中：$i(i=1, 2, \cdots, n)$为控制点序号；(X_{Wi}, Y_{Wi}, Z_{Wi})为全局控制点 i 在世界坐标系下的坐标；(u_i, v_i)为全局控制点 i 在图像坐标系下的像点坐标；(u_0, v_0, f, d_x, d_y)为相机内参。相机坐标系与世界坐标系之间的旋转矩阵 ${}^{C}_{W}\boldsymbol{R}$ 和平移矩阵 ${}^{C}_{W}\boldsymbol{T}$ 可用 6DOF 参数$(\alpha, \beta, \gamma, t_1, t_2, t_3)$表示：

$$\left[{}^{\mathrm{C}}_{\mathrm{W}}\boldsymbol{R}\middle|{}^{\mathrm{C}}_{\mathrm{W}}\boldsymbol{T}\right]=\left[\begin{array}{ccc|c} r_1 & r_2 & r_3 & t_1 \\ r_4 & r_5 & r_6 & t_2 \\ r_7 & r_8 & r_9 & t_3 \end{array}\right]=\left[\begin{array}{ccc|c} \cos\beta\cos\gamma & -\cos\beta\sin\gamma & \sin\beta & t_1 \\ \sin\alpha\sin\beta\cos\gamma+\cos\alpha\sin\gamma & -\sin\alpha\sin\beta\sin\gamma+\cos\alpha\cos\gamma & -\sin\alpha\cos\beta & t_2 \\ -\cos\alpha\sin\beta\cos\gamma+\sin\alpha\sin\gamma & \cos\alpha\sin\beta\sin\gamma+\sin\alpha\cos\gamma & \cos\alpha\cos\beta & t_3 \end{array}\right]。\tag{2}$$

6DOF 参数和物点、像点坐标之间耦合关系复杂，无法写出显示表达式，由式(1)可建立隐函数模型：

$$h(\boldsymbol{P},\boldsymbol{C})=0,\tag{3}$$

$$\begin{cases}\boldsymbol{P}=\left[\alpha,\beta,\gamma,t_1,t_2,t_3\right]^{\mathrm{T}}\\ \boldsymbol{C}=\left[u_1,v_1,\cdots,u_n,v_n,X_{\mathrm{W}1},Y_{\mathrm{W}1},Z_{\mathrm{W}1},\cdots,X_{\mathrm{W}n},Y_{\mathrm{W}n},Z_{\mathrm{W}n}\right]^{\mathrm{T}}\end{cases},\tag{4}$$

式中：$\boldsymbol{C}$为输入量，$\boldsymbol{P}$为输出量。根据隐函数求导法则，得到两者之间的灵敏度系数矩阵为

$$\frac{\partial\boldsymbol{P}}{\partial\boldsymbol{C}}=-\left(\frac{\partial\boldsymbol{h}}{\partial\boldsymbol{P}}\right)^{-1}\left(\frac{\partial\boldsymbol{h}}{\partial\boldsymbol{C}}\right)。\tag{5}$$

对于相机观测到的n个全局控制点，图像平面x和y方向像素误差最小，共存在$2n$个隐函数，将其分别对6个输出量求导，有

$$\frac{\partial\boldsymbol{h}}{\partial\boldsymbol{P}}=\begin{bmatrix} f_x\left(\frac{\partial L_{z1}}{\partial\alpha}\frac{L_{x1}}{L_{z1}^2}-\frac{\partial L_{x1}}{\partial\alpha}\frac{1}{L_{z1}}\right) & f_x\left(\frac{\partial L_{z1}}{\partial\beta}\frac{L_{x1}}{L_{z1}^2}-\frac{\partial L_{x1}}{\partial\beta}\frac{1}{L_{z1}}\right) & f_x\left(\frac{\partial L_{z1}}{\partial\gamma}\frac{L_{x1}}{L_{z1}^2}-\frac{\partial L_{x1}}{\partial\gamma}\frac{1}{L_{z1}}\right) & -\frac{f_x}{L_{z1}} & 0 & \frac{f_xL_{x1}}{L_{z1}^2}\\ f_y\left(\frac{\partial L_{z1}}{\partial\alpha}\frac{L_{y1}}{L_{z1}^2}-\frac{\partial L_{y1}}{\partial\alpha}\frac{1}{L_{z1}}\right) & f_y\left(\frac{\partial L_{z1}}{\partial\beta}\frac{L_{y1}}{L_{z1}^2}-\frac{\partial L_{y1}}{\partial\beta}\frac{1}{L_{z1}}\right) & f_y\left(\frac{\partial L_{z1}}{\partial\gamma}\frac{L_{y1}}{L_{z1}^2}-\frac{\partial L_{y1}}{\partial\gamma}\frac{1}{L_{z1}}\right) & 0 & -\frac{f_y}{L_{z1}} & \frac{f_yL_{y1}}{L_{z1}^2}\\ \vdots & \vdots & \vdots & \vdots & \vdots & \vdots\\ f_x\left(\frac{\partial L_{zn}}{\partial\alpha}\frac{L_{xn}}{L_{zn}^2}-\frac{\partial L_{xn}}{\partial\alpha}\frac{1}{L_{zn}}\right) & f_x\left(\frac{\partial L_{zn}}{\partial\beta}\frac{L_{xn}}{L_{zn}^2}-\frac{\partial L_{xn}}{\partial\beta}\frac{1}{L_{zn}}\right) & f_x\left(\frac{\partial L_{zn}}{\partial\gamma}\frac{L_{xn}}{L_{zn}^2}-\frac{\partial L_{xn}}{\partial\gamma}\frac{1}{L_{zn}}\right) & -\frac{f_x}{L_{zn}} & 0 & \frac{f_xL_{xn}}{L_{zn}^2}\\ f_y\left(\frac{\partial L_{zn}}{\partial\alpha}\frac{L_{yn}}{L_{zn}^2}-\frac{\partial L_{yn}}{\partial\alpha}\frac{1}{L_{zn}}\right) & f_y\left(\frac{\partial L_{zn}}{\partial\beta}\frac{L_{yn}}{L_{zn}^2}-\frac{\partial L_{yn}}{\partial\beta}\frac{1}{L_{zn}}\right) & f_y\left(\frac{\partial L_{zn}}{\partial\gamma}\frac{L_{yn}}{L_{zn}^2}-\frac{\partial L_{yn}}{\partial\gamma}\frac{1}{L_{zn}}\right) & 0 & -\frac{f_y}{L_{zn}} & \frac{f_yL_{yn}}{L_{zn}^2} \end{bmatrix}_{2n\times 6},\tag{6}$$

其中，$L_i\left(L_{xi},L_{yi},L_{zi}\right)(i=1,2,\cdots,n)$表示为

$$\begin{cases}L_{xi}=r_1X_{\mathrm{W}i}+r_2Y_{\mathrm{W}i}+r_3Z_{\mathrm{W}i}+t_1\\ L_{yi}=r_4X_{\mathrm{W}i}+r_5Y_{\mathrm{W}i}+r_6Z_{\mathrm{W}i}+t_2\\ L_{zi}=r_7X_{\mathrm{W}i}+r_8Y_{\mathrm{W}i}+r_9Z_{\mathrm{W}i}+t_3\end{cases}。\tag{7}$$

同理，将$2n$个隐函数对$5n\times 1$维像点和物点坐标向量求导，可得

$$\frac{\partial\boldsymbol{h}}{\partial\boldsymbol{C}}=\begin{bmatrix} 1 & 0 & \cdots & 0 & 0 & A_1 & A_2 & A_3 & \cdots & 0 & 0 & 0\\ 0 & 1 & \cdots & 0 & 0 & B_1 & B_2 & B_3 & \cdots & 0 & 0 & 0\\ \vdots & \vdots & & \vdots & \vdots & \vdots & \vdots & \vdots & & \vdots & \vdots & \vdots\\ 0 & 0 & \cdots & 1 & 0 & 0 & 0 & 0 & \cdots & C_1 & C_2 & C_3\\ 0 & 0 & \cdots & 0 & 1 & 0 & 0 & 0 & \cdots & D_1 & D_2 & D_3 \end{bmatrix}_{2n\times 5n},\tag{8}$$

式中：A_1为$\frac{f_x(r_7L_{x1}-r_1L_{z1})}{L_{z1}^2}$，$A_2$为$\frac{f_x(r_8L_{x1}-r_2L_{z1})}{L_{z1}^2}$，$A_3$为$\frac{f_x(r_9L_{x1}-r_3L_{z1})}{L_{z1}^2}$；$B_1$为$\frac{f_y(r_7L_{y1}-r_4L_{z1})}{L_{z1}^2}$，$B_2$为$\frac{f_y(r_8L_{y1}-r_5L_{z1})}{L_{z1}^2}$，$B_3$为$\frac{f_y(r_9L_{y1}-r_6L_{z1})}{L_{z1}^2}$；$C_1$为$\frac{f_x(r_7L_{xn}-r_1L_{zn})}{L_{zn}^2}$，$C_2$为$\frac{f_x(r_8L_{xn}-r_2L_{zn})}{L_{zn}^2}$，$C_3$为$\frac{f_x(r_9L_{xn}-r_3L_{zn})}{L_{zn}^2}$；$D_1$为$\frac{f_y(r_7L_{yn}-r_4L_{zn})}{L_{zn}^2}$，$D_2$为$\frac{f_y(r_8L_{yn}-r_5L_{zn})}{L_{zn}^2}$，$D_3$为$\frac{f_y(r_9L_{yn}-r_6L_{zn})}{L_{zn}^2}$。

根据不确定度传播定律，相机6DOF位姿不确定度协方差矩阵$\boldsymbol{U}_P$为

$$\boldsymbol{U}_P=\frac{\partial\boldsymbol{P}}{\partial\boldsymbol{C}}\boldsymbol{U}_C\left(\frac{\partial\boldsymbol{P}}{\partial\boldsymbol{C}}\right)^{\mathrm{T}},\tag{9}$$

式中：$\boldsymbol{U}_C$为输入量不确定度协方差矩阵。假设全局控制点的物点和像点观测彼此独立且均满足高斯分布，则含有n个全局控制点观测信息的$\boldsymbol{U}_C$表示为

$$\boldsymbol{U}_C=\mathrm{diag}(\sigma_{u1}^2,\sigma_{v1}^2,\cdots,\sigma_{un}^2,\sigma_{vn}^2,\cdots,\sigma_{X1}^2,\sigma_{Y1}^2,\sigma_{Z1}^2,\cdots,\sigma_{Xn}^2,\sigma_{Yn}^2,\sigma_{Zn}^2)_{5n\times 5n}。\tag{10}$$

将式(6)和式(8)的雅可比矩阵代入式(5)中，可求得输入输出量之间的灵敏度矩阵$\frac{\partial \boldsymbol{P}}{\partial \boldsymbol{C}}$，进而通过式(9)求得$\boldsymbol{U}_P$，则可通过相机观测和位姿求解世界坐标系下的相机6DOF位姿在当前时刻的测量不确定度。

2.3　误差状态扩展卡尔曼滤波模型

误差状态扩展卡尔曼滤波(ESKF)模型通过描述系统误差间接描述系统状态，预测和更新的过程仅针对系统的误差，再用更新后的误差修正系统状态[25]。为实现视觉惯性系统融合定位，建立的卡尔曼滤波器误差状态向量为

$$\delta \boldsymbol{x}=\left\{\delta \boldsymbol{p}^{\mathrm{T}} \quad \delta \boldsymbol{v}^{\mathrm{T}} \quad \delta \boldsymbol{\theta}^{\mathrm{T}} \quad \delta \boldsymbol{b}_{\mathrm{a}}^{\mathrm{T}} \quad \delta \boldsymbol{b}_{\mathrm{w}}^{\mathrm{T}}\right\}, \tag{11}$$

式中：$\delta \boldsymbol{p}$、$\delta \boldsymbol{v}$、$\delta \boldsymbol{\theta}$分别表示系统IMU坐标系下三轴的位置、速度、欧拉角误差；$\delta \boldsymbol{b}_{\mathrm{a}}$和$\delta \boldsymbol{b}_{\mathrm{w}}$表示加速度计和陀螺仪的测量偏差。利用相机观测到的位姿进行卡尔曼滤波的状态更新，将相机位姿转换到IMU初始坐标系下，构建的观测误差向量$\delta \hat{\boldsymbol{z}}$为

$$\delta \hat{\boldsymbol{z}}=\left[\delta \hat{\boldsymbol{z}}_p^{\mathrm{T}} \quad \delta \hat{\boldsymbol{z}}_\theta^{\mathrm{T}}\right]^{\mathrm{T}}=\left[\hat{\boldsymbol{p}}^{\mathrm{T}}-\boldsymbol{p}_{\mathrm{C}}^{\mathrm{T}} \quad \hat{\boldsymbol{\theta}}^{\mathrm{T}}-\boldsymbol{\theta}_{\mathrm{C}}^{\mathrm{T}}\right]^{\mathrm{T}}, \tag{12}$$

式中：$\boldsymbol{p}_{\mathrm{C}}$和$\boldsymbol{\theta}_{\mathrm{C}}$为相机观测的三轴位置和欧拉角；$\hat{\boldsymbol{p}}$和$\hat{\boldsymbol{\theta}}$为IMU经连续时间积分计算的位置和欧拉角。

t_k时刻获取相机观测数据，根据观测误差向量$\delta \hat{\boldsymbol{z}}_k$和上一时刻预测的误差状态向量$\delta \hat{\boldsymbol{x}}_{k/k-1}$更新当前误差状态向量，计算得当前时刻误差状态的最大后验概率的均值为

$$\delta \hat{\boldsymbol{x}}_{k/k}=\delta \hat{\boldsymbol{x}}_{k/k-1}+\boldsymbol{K}_k\left(\delta \hat{\boldsymbol{z}}_k-\boldsymbol{H} \delta \hat{\boldsymbol{x}}_{k/k-1}\right), \tag{13}$$

式中：测量矩阵$\boldsymbol{H}$由单位矩阵和零矩阵构成。卡尔曼增益$\boldsymbol{K}_k$与观测噪声协方差矩阵$\boldsymbol{Q}_k$相关，有

$$\boldsymbol{K}_k=\boldsymbol{P}_{k/k-1} \boldsymbol{H}^{\mathrm{T}}\left(\boldsymbol{H} \boldsymbol{P}_{k/k-1} \boldsymbol{H}^{\mathrm{T}}+\boldsymbol{Q}_k\right)^{-1}。 \tag{14}$$

误差状态向量更新后，当前时刻误差状态向量的协方差矩阵更新为

$$\boldsymbol{P}_{k/k}=\left(\boldsymbol{I}-\boldsymbol{K}_k \boldsymbol{H}\right) \boldsymbol{P}_{k/k-1}\left(\boldsymbol{I}-\boldsymbol{K}_k \boldsymbol{H}\right)^{\mathrm{T}}+\boldsymbol{K}_k \boldsymbol{Q}_k \boldsymbol{K}_k^{\mathrm{T}}。 \tag{15}$$

经过状态更新后，利用当前系统的最大后验概率均值继续预测，直至获取下一次相机观测数据，从而实现误差状态扩展卡尔曼滤波模型下的视觉惯性系统位姿最优估计。

2.4　自适应滤波融合定位模型

ESKF进行状态更新时，依赖于观测信息的协方差矩阵。然而，观测信息的噪声方差会因为测量环境的变化而变化。如果噪声方差不准确，将会直接影响ESKF的精度。本文使用相机提供观测信息，但视觉定位结果往往受测量环境的影响较大，因此当观测条件变差时，视觉定位的精度下降。此时，ESKF中的观测置信度与视觉定位的测量不确定度不匹配，导致ESKF无法实现最优估计。为了解决这个问题，本文提出一种自适应滤波融合定位方法，该方法能够根据观测信息的变化动态调整卡尔曼增益，从而调节对不同信息的信任程度，并减小观测信息噪声变化对滤波融合结果精度的影响。

由于滤波过程状态估计建立在IMU初始坐标系O_{o}-$X_{\mathrm{o}}Y_{\mathrm{o}}Z_{\mathrm{o}}$上，为使坐标系统一，将世界坐标系下的视觉定位不确定度转换至IMU初始坐标系下。O_{b}-$X_{\mathrm{b}}Y_{\mathrm{b}}Z_{\mathrm{b}}$为当前时刻IMU坐标系，$O_{\mathrm{W}}$-$X_{\mathrm{W}}Y_{\mathrm{W}}Z_{\mathrm{W}}$为世界坐标系，$O_{\mathrm{C}}$-$X_{\mathrm{C}}Y_{\mathrm{C}}Z_{\mathrm{C}}$为当前时刻相机坐标系，则世界坐标系下一点$\boldsymbol{P}_{\mathrm{W}i}$在IMU初始坐标系下的坐标为

$$\begin{bmatrix} X_{oi} \\ Y_{oi} \\ Z_{oi} \end{bmatrix}={}_{\mathrm{b}}^{\mathrm{o}}\boldsymbol{R}\left[{}_{\mathrm{C}}^{\mathrm{b}}\boldsymbol{R}\left({}_{\mathrm{W}}^{\mathrm{C}}\boldsymbol{R}\begin{bmatrix} X_{\mathrm{W}i} \\ Y_{\mathrm{W}i} \\ Z_{\mathrm{W}i} \end{bmatrix}+{}_{\mathrm{W}}^{\mathrm{C}}\boldsymbol{T}\right)+{}_{\mathrm{C}}^{\mathrm{b}}\boldsymbol{T}\right]+{}_{\mathrm{b}}^{\mathrm{o}}\boldsymbol{T}, \tag{16}$$

式中：${}_{\mathrm{b}}^{\mathrm{o}}\boldsymbol{R}$和${}_{\mathrm{b}}^{\mathrm{o}}\boldsymbol{T}$为当前IMU坐标系相对初始IMU坐标系的旋转矩阵和平移矩阵，可用6DOF参数$(\varphi, \psi, \kappa, s_1, s_2, s_3)$表示；${}_{\mathrm{C}}^{\mathrm{b}}\boldsymbol{R}$和${}_{\mathrm{C}}^{\mathrm{b}}\boldsymbol{T}$为提前标定好的相机和IMU之间的外参。

根据式(16)建立隐函数模型$g(\boldsymbol{O}, \boldsymbol{P})=0$，其中

$$\begin{cases} \boldsymbol{O}=\left[\varphi, \psi, \kappa, s_1, s_2, s_3\right]^{\mathrm{T}} \\ \boldsymbol{P}=\left[\alpha, \beta, \gamma, t_1, t_2, t_3\right]^{\mathrm{T}} \end{cases}。 \tag{17}$$

IMU初始坐标系下视觉定位测量不确定度$\boldsymbol{U}_O$可以通过灵敏度矩阵和世界坐标系下视觉定位测量不确定度$\boldsymbol{U}_P$求得：

$$\frac{\partial \boldsymbol{O}}{\partial \boldsymbol{P}}=-\left(\frac{\partial \boldsymbol{g}}{\partial \boldsymbol{O}}\right)^{-1}\left(\frac{\partial \boldsymbol{g}}{\partial \boldsymbol{P}}\right), \tag{18}$$

$$\boldsymbol{U}_O=\frac{\partial \boldsymbol{O}}{\partial \boldsymbol{P}} \boldsymbol{U}_P\left(\frac{\partial \boldsymbol{O}}{\partial \boldsymbol{P}}\right)^{\mathrm{T}}。 \tag{19}$$

对式(16)进行化简，得

$$g(\boldsymbol{O}, \boldsymbol{P})={}_{\mathrm{C}}^{\mathrm{o}}\boldsymbol{R}\begin{bmatrix} L_{xi} \\ L_{yi} \\ L_{zi} \end{bmatrix}+{}_{\mathrm{b}}^{\mathrm{o}}\boldsymbol{R}\cdot{}_{\mathrm{C}}^{\mathrm{b}}\boldsymbol{T}+{}_{\mathrm{b}}^{\mathrm{o}}\boldsymbol{T}-\begin{bmatrix} X_{oi} \\ Y_{oi} \\ Z_{oi} \end{bmatrix}=0。 \tag{20}$$

对于n个世界坐标系中的控制点，共有$3n$个隐函数方程，对$\boldsymbol{P}$求导，得

$$\frac{\partial \boldsymbol{g}}{\partial \boldsymbol{P}}=\begin{bmatrix} \left({}_{\mathrm{C}}^{\mathrm{o}}\boldsymbol{R}\dfrac{\partial L_1}{\partial \boldsymbol{P}_\theta}\right)_{3\times 3} & \left({}_{\mathrm{C}}^{\mathrm{o}}\boldsymbol{R}\dfrac{\partial L_1}{\partial \boldsymbol{P}_t}\right)_{3\times 3} \\ \vdots & \vdots \\ \left({}_{\mathrm{C}}^{\mathrm{o}}\boldsymbol{R}\dfrac{\partial L_n}{\partial \boldsymbol{P}_\theta}\right)_{3\times 3} & \left({}_{\mathrm{C}}^{\mathrm{o}}\boldsymbol{R}\dfrac{\partial L_n}{\partial \boldsymbol{P}_t}\right)_{3\times 3} \end{bmatrix}_{3n\times 6}。 \tag{21}$$

对式(16)进行另一种化简，得

$$g(\boldsymbol{O}, \boldsymbol{P})={}_{\mathrm{b}}^{\mathrm{o}}\boldsymbol{R}\begin{bmatrix} G_{xi} \\ G_{yi} \\ G_{zi} \end{bmatrix}+{}_{\mathrm{b}}^{\mathrm{o}}\boldsymbol{T}-\begin{bmatrix} X_{oi} \\ Y_{oi} \\ Z_{oi} \end{bmatrix}=$$
$$\begin{bmatrix} r_{\mathrm{b}1} & r_{\mathrm{b}2} & r_{\mathrm{b}3} \\ r_{\mathrm{b}4} & r_{\mathrm{b}5} & r_{\mathrm{b}6} \\ r_{\mathrm{b}7} & r_{\mathrm{b}8} & r_{\mathrm{b}9} \end{bmatrix}\begin{bmatrix} G_x \\ G_y \\ G_z \end{bmatrix}+\begin{bmatrix} s_1 \\ s_2 \\ s_3 \end{bmatrix}-\begin{bmatrix} X_{oi} \\ Y_{oi} \\ Z_{oi} \end{bmatrix}=0。 \tag{22}$$

对$\boldsymbol{O}$求导，得

$$\frac{\partial g}{\partial O}=\begin{bmatrix}\left(\frac{\partial\left({}^{\circ}_{\mathrm{b}}\boldsymbol{R}\cdot G_1\right)}{\partial \boldsymbol{O}_{\theta}}\right)_{3\times3} & \boldsymbol{I}_{3\times3}\\ \vdots & \vdots\\ \left(\frac{\partial\left({}^{\circ}_{\mathrm{b}}\boldsymbol{R}\cdot G_n\right)}{\partial \boldsymbol{O}_{\theta}}\right)_{3\times3} & \boldsymbol{I}_{3\times3}\end{bmatrix}_{3n\times6}。\tag{23}$$

在已知世界坐标系下的视觉定位测量不确定度$\boldsymbol{U}_P$后，将其转换为IMU初始坐标系下的视觉定位测量不确定度$\boldsymbol{U}_O$。根据ESKF模型，采用相机观测值进行更新，因此$\boldsymbol{Q}_k=\boldsymbol{U}_{O(t=t_k)}$。

将$\boldsymbol{U}_O$代入式(14)，即在视觉定位准确即视觉定位测量不确定度小时，$\boldsymbol{K}_k$较大，增大了相机观测对ESKF结果的影响；在视觉定位不准确即视觉定位测量不确定度大时，$\boldsymbol{K}_k$较小，减小了相机观测对ESKF结果的影响。因此，这样实现了运动过程中可动态调节的实时自适应滤波融合，增强了系统定位鲁棒性，提高了系统的定位精度和测量精度。

3　实验与分析

为验证所提自适应滤波融合定位模型算法的可行性和定位精度，搭建如图3所示的实验平台，包括融入式测量定位头盔、精密三轴转台、全局控制场、激光跟踪仪T-mac位姿测量系统、V-STARS摄影测量系统等。采用Xsens公司的MTi-10系列IMU，Basler dart系列的daA1600-60 μm相机和UP Xtreme系列Windows开发板，开发板作为上位机实时对相机和IMU数据进行采集和处理。全局控制场由刚体架(尺寸为3 m×2 m)和15个全局控制板组成，每个全局控制板上粘有V-STARS编码点以及嵌入了波长为890 nm的红外LED(全局控制点)，两者的位置关系提前经过影像仪标定。头盔和T-mac固定在精密三轴转台上，刚体架距精密三轴转台约4 m。精密三轴转台带动头盔和T-mac进行旋转，运动过程中两者的相对位置保持不变。激光跟踪仪(AT960)对T-mac的姿态测量精度为0.01°，位置测量精度为15 μm+6 μm/m，以此测量结果作为标准来评定融入式测量定位头盔的定位精度。

使用V-STARS测量相机拍摄全局控制板，建立世界坐标系，得到全局控制点在世界坐标系下的坐标。激光跟踪仪和V-STARS通过观测相同点得到坐标系转换关系，进而将世界坐标系下头盔定位系统的位姿转换至激光跟踪仪坐标系下，和T-mac位姿匹配，实现定位精度验证。在图3所示实验现场，设置相机拍摄频率为20 Hz，IMU测量频率为200 Hz并同步触发，精密三轴转台的外框以5 (°)/s速度进行旋转。如图4所示，在系统运动过程中根据隐函数模型求解视觉定位不确定度，一共求得运动过程中268个时刻头盔测量系统的三轴位置和三轴角度测量不确定度，为避免刻度差别过大，将协方差表征的不确定度开平方表示。

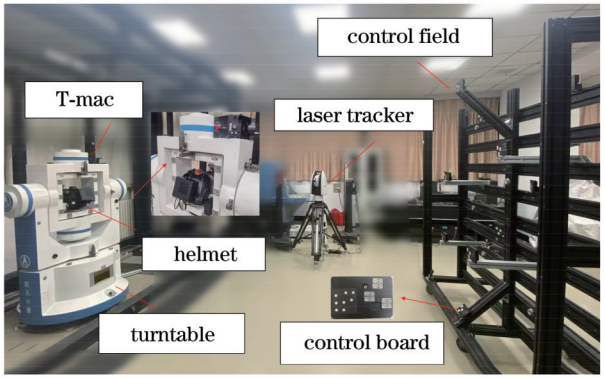

图3　实验场景

Fig. 3　Experiment scene

转台带动头盔运动过程中，相机视场从全局控制场边缘移到中央再到边缘，当运动到中间位置(测量序列84～160)时，视觉定位测量不确定度最小；在运动初始和结束位置，只有一部分控制点处于相机视场的边缘，尤其在结束位置(测量序列219～268)，相机视场内仅拍摄到三个控制点，三对点的PnP方法求解的相机位姿缺少冗余信息约束，视觉定位测量不确定度明显增大。

V-STARS测量相机和激光跟踪仪通过观测公共特征点进行最佳拟合转换，获得世界坐标系和激光跟踪仪坐标系的转换关系，如表1所示，进而将世界坐标系下的系统位姿转换至激光跟踪仪坐标系下。图5为实验场景下T-mac和头盔测量系统的运动轨迹，两者都随转台外框旋转，运动轨迹为一段圆弧。运动轨迹可以直观地反映所求位置准确程度，图6分别画出了纯视觉定位、传统扩展卡尔曼滤波和所提方法求得的激光跟踪仪坐标系下头盔系统的运动轨迹。由图6可知，运动结束时刻，视觉定位测量不确定度较大，纯视觉定位和ESKF运动轨迹偏离和波动较大，所提方法求得的轨迹更加还原真实运动。

测量过程中可同时获得激光跟踪仪坐标系下T-mac和头盔测量系统的位姿。在实际测量时，T-mac和头盔测量系统的相对位姿关系固定不变，但由于测量误差存在，求得的结果并非定值。图7为所提方法求得的运动过程中268个时刻头盔测量系统相对于T-mac的位姿，由图7可知，三轴欧拉角和位置在一定范围内波动，在视觉定位测量不确定度较小的位置相对位姿波动幅度较小，在视觉定位测量不确定度较大的位置相对位姿波动幅度较大。

以标准偏差衡量相对位姿的分散程度，以此来评价头盔测量系统的位姿测量精度。结合视觉定位测量不确定度，分别评价测量序列中视觉定位测量不确定度较小的运动轨迹(测量序列84～160)和视觉定位测量不确定度较大的运动轨迹(测量序列219～268)，如表2和表3所示，表中分别列出了纯视觉定位、传统扩展卡尔曼滤波、所提方法获得的相对位姿的标准偏差。

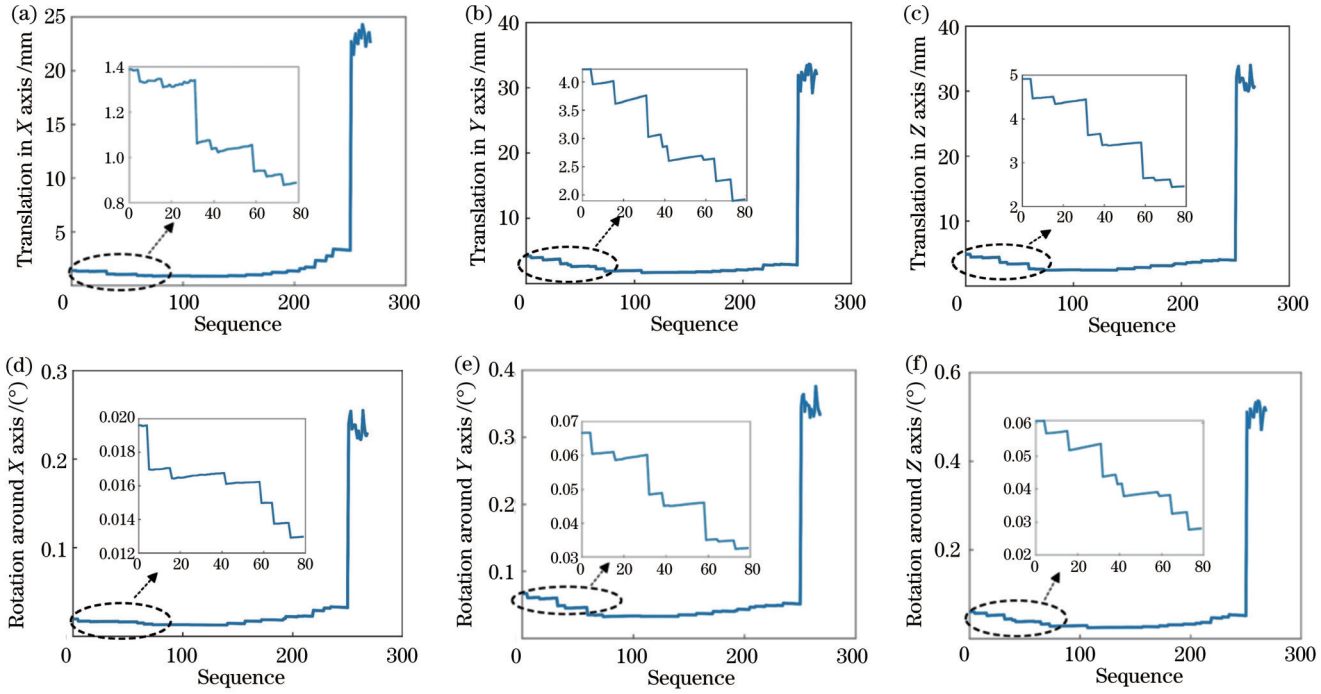

图 4　视觉定位测量不确定度。(a)X轴方向平移;(b)Y轴方向平移;(c)Z轴方向平移;(d)X轴方向旋转;(e)Y轴方向旋转;(f)Z轴方向旋转

Fig. 4　Measurement uncertainty of visual positioning. (a) Translation in X axis; (b) translation in Y axis; (c) translation in Z axis; (d) rotation around X axis; (e) rotation around Y axis; (f) rotation around Z axis

表 1　世界坐标系到激光跟踪仪坐标系的外参

Table 1　Extrinsic parameters from world coordinate system to laser tracker coordinate system

Rotation matrix			Translation vector
0.1638	−0.0050	−0.9865	−960.3510
0.9865	−0.0038	0.1638	−2095.5485
−0.0046	−0.1000	0.0043	−68.8629

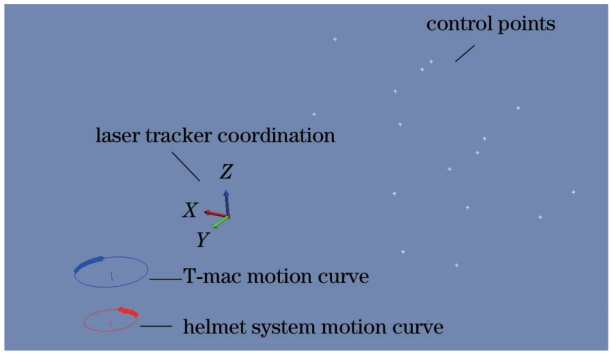

图 5　T-mac 和头盔测量系统的运动轨迹

Fig. 5　Motion curve of T-mac and helmet system

其中R_x、R_y、R_z表示绕三轴旋转欧拉角的标准偏差,T_x、T_y、T_z表示三轴位置标准偏差。由表 2 可知,所提自适应滤波融合方法的各轴角度标准偏差小于 0.04°,各轴位置标准偏差不超过 2 mm。可以看出,在视觉定位测量不确定度小时,纯视觉定位、传统扩展卡尔曼滤波和

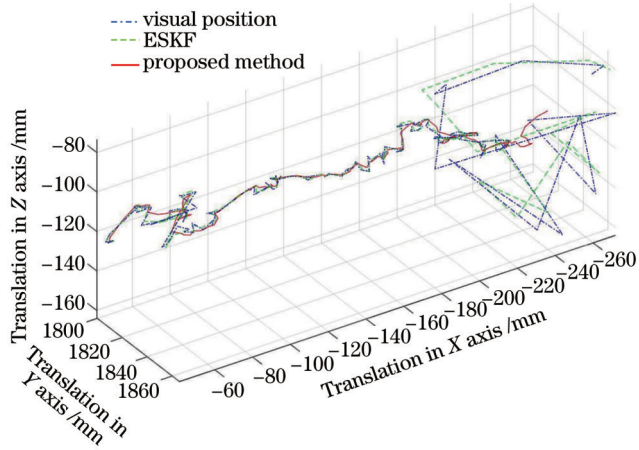

图 6　纯视觉定位、ESKF 和所提方法获得的运动轨迹

Fig. 6　Motion curves of visual position, ESKF, and proposed method

所提方法都能取得较好的定位结果。由表 3 可知,所提自适应滤波融合方法得到的各轴角度标准偏差小于 0.2°,各轴位置标准偏差不超过 7 mm。可以看出:在视觉定位测量不确定度大时,纯视觉定位和传统扩展卡尔曼滤波的定位结果偏差较大;所提方法沿x轴的角度标准偏差与传统扩展卡尔曼滤波相当,y轴和z轴分别降低了 46.4% 和 28.7%,三轴位置标准偏差分别降低 66.4%、60.4%、43.7%,所提方法提升了视觉观测条件较差情况下的定位精度。

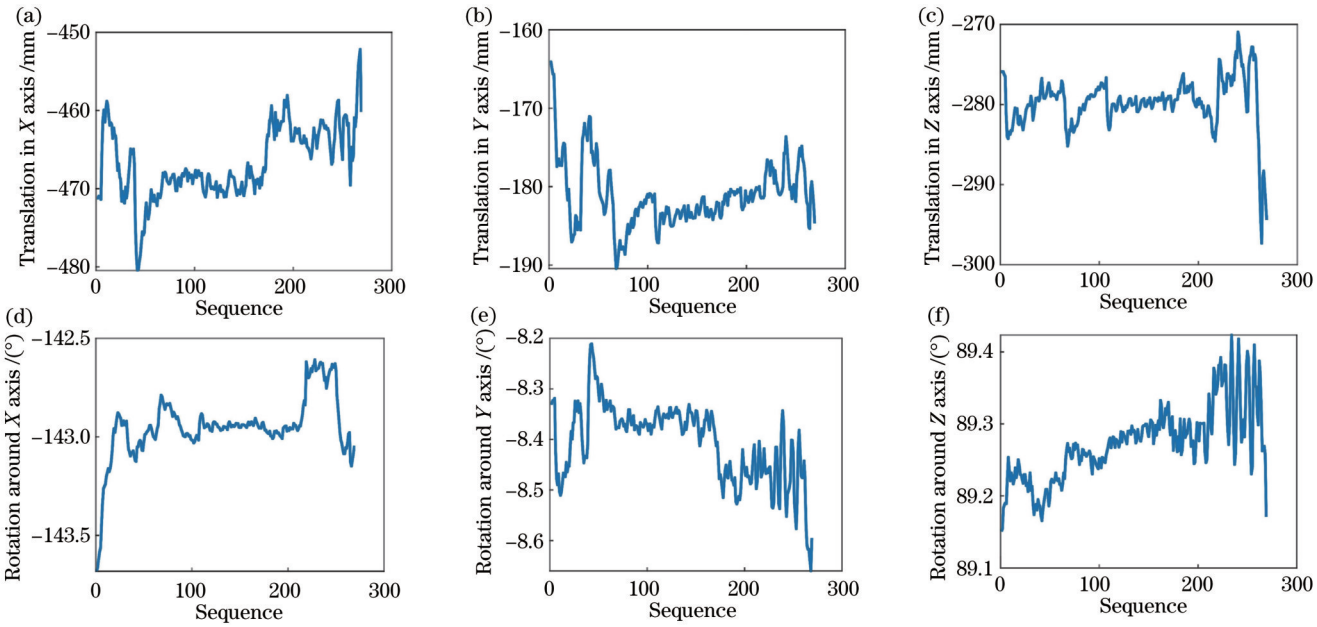

图 7　T-mac 和头盔测量系统的相对位姿。(a)X轴方向平移;(b)Y轴方向平移;(c)Z轴方向平移;(d)X轴方向旋转;(e)Y轴方向旋转;(f)Z轴方向旋转

Fig. 7　Relative pose between T-mac and helmet system. (a) Translation in X axis; (b) translation in Y axis; (c) translation in Z axis; (d) rotation around X axis; (e) rotation around Y axis; (f) rotation around Z axis

表 2　视觉定位测量不确定度小的测量序列相对位姿标准偏差

Table 2　Standard deviation of relative pose of measurement sequence with small uncertainty of visual positioning

Standard deviation	Visual position	ESKF	Proposed method
R_x /(°)	0.0332	0.0314	0.0318
R_y /(°)	0.0192	0.0165	0.0172
R_z /(°)	0.0175	0.0194	0.0189
T_x /mm	1.3196	1.1995	1.1062
T_y /mm	1.4611	1.4019	1.3540
T_z /mm	1.1937	1.1636	1.1492

表 3　视觉定位测量不确定度大的测量序列相对位姿标准偏差

Table 3　Standard deviation of relative pose of measurement sequence with large uncertainty of visual positioning

Standard deviation	Visual position	ESKF	Proposed method
R_x /(°)	0.2149	0.1837	0.1858
R_y /(°)	0.1510	0.1341	0.0719
R_z /(°)	0.0718	0.0735	0.0524
T_x /mm	11.3176	9.8335	3.3020
T_y/mm	7.2154	6.4384	2.5462
T_z /mm	11.9169	10.9746	6.1778

4　结　　论

工业现场环境复杂,难以保证相机观测一直处于较好情况,纯视觉定位和传统扩展卡尔曼滤波算法需要良好的相机观测条件才能获得准确的位姿估计。所提基于视觉定位测量不确定度的自适应滤波融合定位算法能在相机观测条件较差的情况下提供比纯视觉定位和传统扩展卡尔曼滤波算法更优的位姿融合结果。所提算法通过求解视觉定位测量的不确定度,及时调整相机观测信息的权重,更好地适应不同的观测条件,增强系统的定位鲁棒性,并提高滤波方法的视觉惯性定位测量精度,满足了复杂工业场景中融入式测量定位的需求。

参　考　文　献

[1] 尹仕斌, 任永杰, 刘涛, 等. 机器视觉技术在现代汽车制造中的应用综述[J]. 光学学报, 2018, 38(8): 0815001.
Yin S B, Ren Y J, Liu T, et al. Review on application of machine vision in modern automobile manufacturing[J]. Acta Optica Sinica, 2018, 38(8): 0815001.

[2] 魏振忠, 冯广堃, 周丹雅, 等. 位姿视觉测量方法及应用综述[J]. 激光与光电子学进展, 2023, 60(3): 0312010.
Wei Z Z, Feng G K, Zhou D Y, et al. Summary of position and attitude vision measurement methods and applications[J]. Laser & Optoelectronics Progress, 2023, 60(3): 0312010.

[3] 郭金辉, 陈秀万, 王媛. 视觉惯性SLAM研究进展[J]. 火力与指挥控制, 2021, 46(1): 1-8.
Guo J H, Chen X W, Wang Y. A review of visual inertial SLAM research development[J]. Fire Control & Command Control, 2021, 46(1): 1-8.

[4] Sun K, Mohta K, Pfrommer B, et al. Robust stereo visual inertial odometry for fast autonomous flight[J]. IEEE Robotics and Automation Letters, 2018, 3(2): 965-972.

[5] 褚金奎, 胡瀚珮, 万振华, 等. 偏振光辅助的视觉惯性导航系统[J]. 激光与光电子学进展, 2023, 60(7): 0726002.
Chu J K, Hu H P, Wan Z H, et al. Visual inertial navigation system aided by polarized light[J]. Laser & Optoelectronics Progress, 2023, 60(7): 0726002.

[6] 王柏村, 黄思翰, 易兵, 等. 面向智能制造的人因工程研究与

发展[J]. 机械工程学报, 2020, 56(16): 240-253.
Wang B C, Huang S H, Yi B, et al. State-of-art of human factors/ergonomics in intelligent manufacturing[J]. Journal of Mechanical Engineering, 2020, 56(16): 240-253.
[7] 徐秋宇. 面向融入式测量的多相机视觉定位系统整体标定方法[D]. 天津: 天津大学, 2018.
Xu Q Y. Integral calibration method of multi-camera visual positioning system for integrated measurement[D]. Tianjin: Tianjin University, 2018.
[8] Male J, Martinez-Hernandez U. Recognition of human activity and the state of an assembly task using vision and inertial sensor fusion methods[C]//2021 22nd IEEE International Conference on Industrial Technology (ICIT), March 10-12, 2021, Valencia, Spain. New York: IEEE Press, 2021: 919-924.
[9] 司书斌, 赵大伟, 徐婉莹, 等. 视觉—惯性导航定位技术研究进展[J]. 中国图象图形学报, 2021, 26(6): 1470-1482.
Si S B, Zhao D W, Xu W Y, et al. Review on visual-inertial navigation and positioning technology[J]. Journal of Image and Graphics, 2021, 26(6): 1470-1482.
[10] Qin T, Li P L, Shen S J. VINS-mono: a robust and versatile monocular visual-inertial state estimator[J]. IEEE Transactions on Robotics, 2018, 34(4): 1004-1020.
[11] Campos C, Elvira R, Rodríguez J J G, et al. ORB-SLAM3: an accurate open-source library for visual, visual-inertial, and multimap SLAM[J]. IEEE Transactions on Robotics, 2021, 37(6): 1874-1890.
[12] Leutenegger S, Lynen S, Bosse M, et al. Keyframe-based visual-inertial odometry using nonlinear optimization[J]. The International Journal of Robotics Research, 2015, 34(3): 314-334.
[13] Li M Y, Mourikis A I. High-precision, consistent EKF-based visual-inertial odometry[J]. The International Journal of Robotics Research, 2013, 32(6): 690-711.
[14] Bloesch M, Omari S, Hutter M, et al. Robust visual inertial odometry using a direct EKF-based approach[C]//2015 IEEE/RSJ International Conference on Intelligent Robots and Systems (IROS), September 28-October 2, 2015, Hamburg, Germany. New York: IEEE Press, 2015: 298-304.
[15] Weiss S M. Vision based navigation for micro helicopters[D]. Zurich: ETH Zurich, 2012.
[16] Lynen S, Achtelik M W, Weiss S, et al. A robust and modular multi-sensor fusion approach applied to MAV navigation[C]//2013 IEEE/RSJ International Conference on Intelligent Robots and Systems, November 3-7, 2013, Tokyo, Japan. New York: IEEE Press, 2014: 3923-3929.
[17] 张礼廉, 屈豪, 毛军, 等. 视觉/惯性组合导航技术发展综述[J]. 导航定位与授时, 2020, 7(4): 50-63.
Zhang L L, Qu H, Mao J, et al. Review on the development of vision/inertial integrated navigation technology[J]. Navigation Positioning and Timing, 2020, 7(4): 50-63.
[18] Wang X Y, Zhu Z M, Zhou F Q, et al. Complete calibration of a structured light stripe vision sensor through a single cylindrical target[J]. Optics and Lasers in Engineering, 2020, 131: 106096.
[19] Zhu Z M, Liu Q X, Wang X Y, et al. Distortion correction method of a zoom lens based on the vanishing point geometric constraint[J]. Measurement Science and Technology, 2019, 30(10): 105402.
[20] Zhu Z M, Wang X Y, Liu Q X, et al. Camera calibration method based on optimal polarization angle[J]. Optics and Lasers in Engineering, 2019, 112: 128-135.
[21] Eckenhoff K, Geneva P, Bloecker J, et al. Multi-camera visual-inertial navigation with online intrinsic and extrinsic calibration[C]//2019 International Conference on Robotics and Automation (ICRA), May 20-24, 2019, Montreal, QC, Canada. New York: IEEE Press, 2019: 3158-3164.
[22] Furgale P, Rehder J, Siegwart R. Unified temporal and spatial calibration for multi-sensor systems[C]//2013 IEEE/RSJ International Conference on Intelligent Robots and Systems, November 3-7, 2013, Tokyo, Japan. New York: IEEE Press, 2014: 1280-1286.
[23] 马可瑶, 任永杰, 林嘉睿, 等. 一种视觉惯性系统位姿高精度一体化标定方法[J]. 激光与光电子学进展, 2023, 60(3): 0312021.
Ma K Y, Ren Y J, Lin J R, et al. High-precision integrated calibration method for position and attitude of visual inertial system[J]. Laser & Optoelectronics Progress, 2023, 60(3): 0312021.
[24] Niu Z Y, Yang L H, Ren Y J, et al. Robust 6DOF measurement for non-overlapping multi-camera systems based on uncertainty-weighted space resection[J]. Proceedings of SPIE, 2020, 11439: 114391I.
[25] Madyastha V, Ravindra V, Mallikarjunan S, et al. Extended Kalman filter *vs.* error state Kalman filter for aircraft attitude estimation[C]//AIAA Guidance, Navigation, and Control Conference, August 8-11, 2011, Portland, Oregon. Virginia: AIAA Press, 2011: 6615.

Visual-Inertial Adaptive Fusion Algorithm Based on Measurement Uncertainty

Huang Xinxin, Ren Yongjie*, Ma Keyao, Niu Zhiyuan

State Key Laboratory of Precision Measurement Technology and Instrument, Tianjin University, Tianjin 300072, *China*

Abstract

Objective In recent years, with the development of computer vision, image processing, data fusion, and other technologies, visual measurement has been widely applied in various fields of modern industry. The inertial measurement unit (IMU) has fast response speed, good dynamic performance, and high short-term accuracy, which can well improve the robustness of visual positioning in complex industrial environments represented by large-scale equipment manufacturing sites such as shipbuilding and aerospace. However, traditional filtering-based visual-inertial fusion algorithms maintain the fusion weights of visual and inertial information unchanged. When visual observation conditions are poor, traditional

algorithms will greatly reduce the accuracy of visual-inertial positioning. Therefore, in order to solve the problems of low accuracy, poor adaptability, and low robustness caused by poor visual observation conditions in complex industrial environments, we propose a visual-inertial adaptive fusion algorithm based on measurement uncertainty. To address the situation of poor visual observation conditions, we dynamically adjust the data fusion weights of the visual sensor and inertial sensor by analyzing the measurement uncertainty of visual positioning. It can greatly improve measurement accuracy while enhancing measurement robustness.

Methods In order to complete the real-time assembly and positioning tasks of large-scale and complex equipment such as spacecraft and ship hulls, we use a wearable helmet as the carrier, combined with immersive measurement technology, and calibrate the visual-inertial system by using a three-axis precision turntable. Loosely coupled filtering is used to fuse visual and inertial information, and real-time global pose estimation of the surveyor is obtained. In this paper, the measurement uncertainty of visual positioning based on the implicit function model is analyzed. The global control point position error and the image point extraction error are taken as the input of the uncertainty propagation model, and the measurement uncertainty of visual positioning is obtained as the output. Then, the error state extended Kalman filter (ESKF) is used to achieve visual-inertial fusion localization. Updating the state of ESKF relies on the covariance matrix of observation information, which directly affects the accuracy of ESKF. We also use cameras to provide observation information, but the visual positioning results are often greatly affected by the measurement environment. When the observation condition is poor, the accuracy of visual positioning decreases, and the observation confidence in ESKF does not match the measurement uncertainty of visual positioning, resulting in the inability of ESKF to achieve optimal estimation. In order to adapt to different visual observation conditions, we establish an adaptive filtering fusion positioning model. The observation noise covariance matrix in the ESKF model is represented by the measurement uncertainty of visual positioning, so the fusion weights of visual and inertial information in the ESKF model are adaptively adjusted. When the measurement uncertainty of visual positioning is small, which means that visual positioning is accurate, the Kalman gain is large, increasing the influence of camera observation on ESKF results. When the measurement uncertainty of visual positioning is large, which means that visual positioning is inaccurate, the Kalman gain is small, reducing the influence of camera observation on ESKF results.

Results and Discussions We use a T-mac pose measurement system of the laser tracker and a precision three-axis turntable to experimentally verify the positioning accuracy of the proposed fusion positioning algorithm (Fig. 3). In the process of system movement, the visual positioning uncertainty is solved according to the implicit function model (Fig. 4), and it is substituted for the covariance matrix of observation information of ESKF model to obtain the results of the proposed method. In the actual measurement, the relative pose between T-mac and helmet measurement system remains fixed, but due to measurement errors, the results obtained are not fixed. The standard deviation is used to measure the dispersion degree of relative pose to evaluate the pose measurement accuracy of the helmet measurement system. Compared with the results obtained by pure visual positioning and traditional ESKF (Fig. 6), when the measurement uncertainty of visual positioning is small, and the visual observation condition of the proposed method is good (Table 2), the standard deviation of each axis angle is less than 0.04°, and the standard deviation of each axis position is less than 2 mm. All three methods can get good positioning results. When the measurement uncertainty of visual positioning is large, and the visual observation condition is poor (Table 3), the positioning results of pure visual positioning and traditional ESKF have a significant deviation. In addition, by using the proposed method, the standard deviation of each axis angle is less than 0.2°, and the standard deviation of each axis position is less than 7 mm. Compared with the traditional ESKF method, the standard deviation of the three-axis angle of the proposed method decreases by 46.4% and 28.7% except for the X-axis, and the standard deviation of the three-axis position decreases by 66.4%, 60.4%, and 43.7%

Conclusions The industrial environment is complex, so it is difficult to ensure that visual observation is always in good condition. Pure visual positioning and traditional ESKF methods require good visual observation conditions to obtain accurate pose estimation. The visual-inertial adaptive fusion algorithm based on measurement uncertainty proposed in this paper can provide better pose fusion results than pure visual positioning and traditional ESKF methods under poor visual observation conditions. The proposed method adjusts the weight of camera observation information in a timely manner, better adapts to different observation conditions, enhances the positioning robustness of the system, and improves the accuracy of filtering-based visual inertial positioning measurement by solving the measurement uncertainty of visual positioning, so it meets the needs of visual-inertial positioning in complex industrial environments.

Key words measurement; Kalman filtering; uncertainty analysis; visual-inertial fusion; pose measurement